# Synthesis, Characterisation, Magnetic Properties, and DFT Investigations of Heterobimetallic Nickel-Lanthanide LNiIILnIII (Ln = Ce, Gd, Tb, Dy) Complexes Supported by Schiff Base Ligands

Fatma Darkebira, Fatema Zohra Chiboub-Fellah, Lotfi Belkhiri, Thierry Roisnel, Souhir El Hassasna, Thierry Guizouarn, Abdou Boucekkine, Fabrice Pointillart

# Synthesis, Characterisation, Magnetic Properties, and DFT Investigations of Heterobimetallic Nickel-Lanthanide $LNi^{II}Ln^{III}$ (Ln = Ce, Gd, Tb, Dy) Complexes Supported by Schiff Base Ligands

Fatma Darkebira,[a] Fatéma Zohra Chiboub Fellah,*[a] Lotfi Belkhiri,[b],[c] Thierry Roisnel,[d] Souhir El Hassasna,[d],[e] Thierry Guizouarn,[d] Abdou Boucekkine,[d] Fabrice Pointillart*[d]

[a] F. Darkebira, Prof. F. Z. Chiboub Fellah,
Laboratory of Inorganic Chemistry and Environment, University of Tlemcen, BP119, 13000 Tlemcen, Algeria.
E-mail: cfatema@yahoo.fr
[b] L. Belkhiri
Laboratoire de Physique Mathématique et Subatomique LPMS, Département de Chimie, Université Constantine 1 des Frères Mentouri , 25017, Algeria.
[c] L. Belkhiri
Centre de Recherche en Sciences Pharmaceutiques CRSP, ZAM Ali Mendjeli, 25000 Constantine, Algeria.
[d] Dr. T. Roisnel, Dr. S. El Hassasna, T. Guizouarn, Prof. A. Boucekkine, Dr. F. Pointillart
Univ Rennes, CNRS, ISCR (Institut des Sciences Chimiques de Rennes) - UMR 6226, 35042 Rennes, France.
E-mail: fabrice.pointillart@univ-rennes.fr
[e] Dr. S. El Hassasna
Université de Echahid Cheikh Larbi Tébessi, Tébessa, route de Constantine, 12022, Tébessa, Algeria.

Supporting information for this article is given via a link at the end of the document.

**Abstract:** Four heterobimetallic complexes (Ln = Ce (**2**), Gd (**3**), Tb (**4**), and Dy (**5**), $H_2L$= Schiff base ligand) were synthesized from LNi (**1**) precursor ($H_2L$ = ligand N, N'-bis(3-methoxysalicylaldiimine)-1,3-propylene-2-ol). Compound **2**, which crystallizes in the tetragonal system, differs from the other isostructural **3**, **4**, and **5** congeners which crystallize in the monoclinic system. The dc magnetic studies revealed ferromagnetic interaction between the Ni(II) (S = 1) and the lanthanide (Ln(III) = Gd, Tb and Dy) but not for Ce(III) in agreement with the computational results. The dynamic magnetic investigations highlighted field-induced Single-Molecule Magnet (SMM) behaviours for Ln(III) = Ce, Tb and Dy. In case of compound **4**, it was determined that the slow magnetic relaxation occurred through an Orbach process only with $\Delta$ = 19.1(3) K and $\tau_0 = 3.99(4) \times 10^{-7}$ s (H = 1200 Oe). Electronic structures and magnetic properties have been investigated theoretically using Relativistic Density Functional Theory (DFT) calculations combined with the Broken Symmetry (BS) approach for the magnetic properties. Moreover, the computed Mayer and Nalewajski-Mrozek (NM) Ni(II)–$O_b$ and $O_b$–Ln(III) bond orders are found to be higher for **2** than for **3**, **4**, and **5**, correlating well with the AF and Ferro character of each species.

## Introduction

Lanthanide ions are the most promising candidates for the observation of slow magnetic relaxation behaviour due to their specific magnetic characteristic i.e. high magnetic moment and strong magnetic anisotropy.[1] In this context, design of organometallic complexes involving lanthanide ions allowed the observation of Single-Molecule Magnet (SMM) behaviour with magnetic bistability up to 80 K.[2] Such magnetic performances make such systems suitable for potential applications in high-density data storage devices but also for quantum computing and spintronics.[3-5] One of the drawback to obtain high performance SMMs is the fast magnetic relaxation through quantum tunnelling of the magnetization (QTM). One way to cancel the latter is to impose significant magnetic interaction between the spin carriers. Thus, chemists in the molecular magnetism field, design polynuclear lanthanide complexes[6,7] or 3d4f heterobimetallic complexes.[8-12] For the latter kind of compounds, stronger exchange magnetic interactions are observed compared to pure lanthanide polynuclear systems.
In recent years, cerium(III) has emerged as a promising metallic center for designing molecular systems with SMM behavior.[13-23] Despite having a single 4f electron, numerous studies have explored cerium in both monometallic[24] and polymetallic complexes[25,26], particularly with diamagnetic zinc[24],[27]. In order to investigate its interactions with nickel and compare it to the other lanthanides, this study synthesized, characterized, and crystallized four Schiff base complexes LNi-Ln **2**, **3**, **4**, and **5** (Ln: Ce, Gd, Tb, and Dy), where $H_2L$ is N,N'-bis(3-methoxysalicylaldimine)-1,3-propylene-2-ol. The synthesis and structure of compound **2** deviate from those of the other three, which are isostructural.

Although nickel, with its $d^8$ configuration, generally adopts a square planar geometry with $dsp^2$ hybridization,[28-31] in these complexes nickel prefers an octahedral geometry with $sp^3d^2$ hybridization. This six-coordinate geometry is favored in dinuclear complexes when the metal is coordinated to multiple ligands or to flexible diamines[32-37] as well as to ligands containing tri- or tetra-amines[38, 39]. In contrast, trinuclear NiLnNi complexes usually maintain a coordination number of four, regardless of the ligand.[40] By replacing nickel with another 3d metal, specifically copper and zinc, these are generally penta-coordinated, whether for di-, tri-, or tetranuclear (3d–4f) complexes.[41-45]

In complex (**2**), the nickel is surrounded by four oxygens and two nitrogen atoms from the diamine, which are in cis positions. In contrast, the other three isostructural complexes exhibit a fac-isomeric arrangement, with the nickel ion coordinated to three nitrogen atoms and three oxygen atoms, positioned at the vertices of two opposite triangular faces of the octahedron, analogous to our previously reported complexes.[36] The lanthanide ion in all four compounds is coordinated by ten oxygen atoms, a typical coordination number for such complexes.[46]

The nature of the 3d–4f magnetic interactions within the $[Ni^{II}(\mu\text{-}O)_2Ln^{III}]$ core (Ln = Ce, Gd, Tb, Dy) has been investigated using scalar relativistic ZORA/DFT calculations and the GGA BP86 functional for geometry optimization. To compute the exchange coupling constant J($cm^{-1}$), the two hybrid B3LYP and PBE0 methods have been used in combination with the Broken Symmetry (BS) approach. To our knowledge, no systematic theoretical study has been carried out up to now for these species. The ZORA/BP86/TZP geometry optimizations were carried out based on the X-ray structures of these species, keeping fixed the crystals $[Ni^{II}(\mu\text{-}O)_2Ln^{III}]$ core structures.

In these $Ni^{II}Ln^{III}$ systems, the structures are built up by [NiL] unit bound to the central Lanthanide(III) $Ln(NO_3)n^{+/0}$ (n = 2, 3) ion by two pairs of oxygen atoms, leading to the $[Ni(\mu O_b)_2]_2Ln]$ cores, as shown on Figure 1.

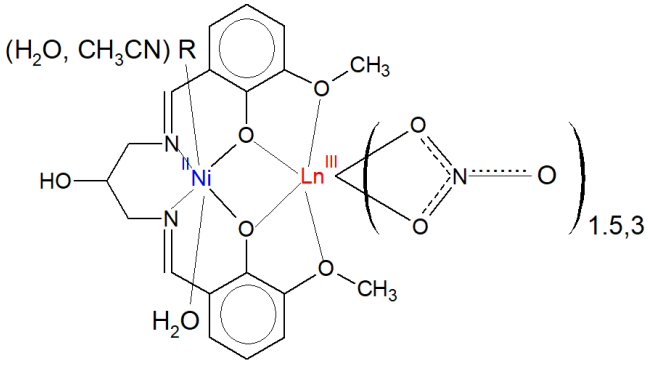


Figure 1: Molecular structure of the $[LNi^{II}Ln^{III}]^{+/0}$ (Ln = Ce, Gd, Tb, Dy) complexes.

## Results and Discussion

### Description of crystal structures

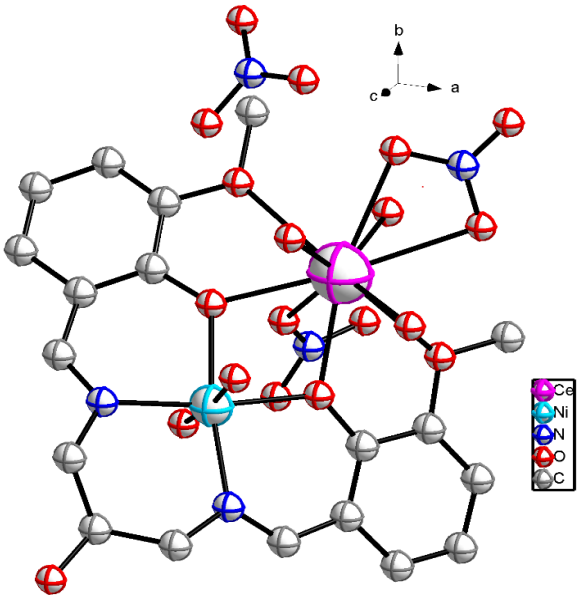


Figure 2 shows the asymmetric unit of complex **2**, which crystallizes in the tetragonal system, space group I41cd (no. 110) with Z = 16 (Table S1). Selected metric parameters pertaining to all structures are listed in Figure S2. The compound is composed of a nitrate anion ($NO_3^-$) and a dinuclear Ni-Ce cation. The nickel center adopts a slightly distorted octahedral geometry, similar to structures possessing the same ligand but differing in nuclearity.[47] It is coordinated to two oxygen and two nitrogen atoms from the ligand in equatorial positions (Ni-O/N = 2.019(7)-2.038(6) Å) and to two oxygen atoms from water molecules in axial positions (Ni-O = 2.095(7), 2.113(6) Å).

Figure 2: Molecular structure of (**2**), Hydrogen atoms are omitted for clarity.

The two diamine nitrogens are in cis position with a bite angle N36Ni1N31 equal to 98.6(3)°. The O61-Ni-O62 linkage exhibits a slight bend with a bond angle of 174.5° (3). The Nickel atom displays a deviation of 0.0228 Å from the plane formed by the two equatorial oxygen and nitrogen atoms. The second metal center, Ce, located 3.550(2) Å from Ni, is coordinated to ten oxygen atoms. Four of these are from the ligand, three from water molecules, and three from two nitrate anions (one monodentate and one bidentate). Ce-O bond lengths range from 2.401(6) to 2.740(6) Å. The Ni-O-Ce angles: Ni1O44Ce1 and Ni1O29Ce1, are 105.2(2)° and 106.0(2)°, respectively. The angle between the two planes formed by nickel and its four nearest neighbors from the ligand and cerium and its four surrounding oxygens from the ligand is equal to 9.7(2)°. Numerous intra- and intermolecular hydrogen bonds are present, as illustrated in the (100) plane of the complex (Figure S2). Specific details of these interactions are provided in Table S2.

Complex **3**, consisting of a neutral asymmetric unit, crystallizes in space group P $2_1/c$ (no. 14) of the monoclinic system with Z = 4, and is shown in Figure 3. The asymmetric unit contains two metal centers, Ni and Gd, separated by 3.516(5) Å. As in the previous complex, the nickel center adopts a distorted octahedral geometry, coordinated by two nitrogen and two oxygen atoms from the ligand (Ni-N/O = 2.015(2)-2.039(2) Å) in equatorial positions. The axial sites are

coordinated by an oxygen atom from water and a nitrogen atom from acetonitrile. The Ni-N bond (2.112(3) Å) is slightly longer than the Ni-O bond (2.094(2) Å). The nickel center adopts a fac isomerism, with two triangular faces of the octahedron occupied by either three oxygen or three nitrogen atoms. The gadolinium ion is coordinated to ten oxygen atoms: four from the ligand (Gd-O = 2.327(2)-2.553(2) Å) and six from three bidentate nitrates (Gd-O = 2.432(2)-2.540(2) Å). The Ni-O-Gd angles, Ni2O54Gd1 and Ni2O39Gd1, are 107.93(9)° and 106.84(9)°, respectively.

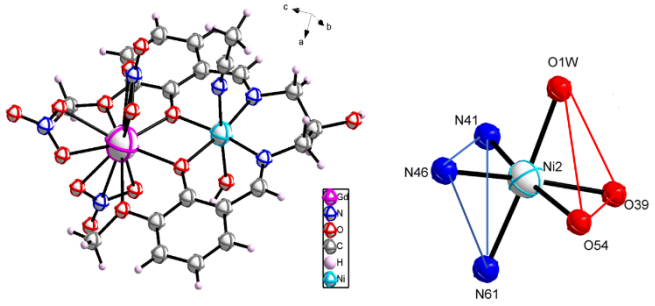


**Figure 3**: (left) Asymmetric unit of complex **3** depicted with hydrogen atoms omitted for clarity. (right) Fac isomeric form adopted by the nickel's immediate environment of (**3**)

Three intermolecular hydrogen bonds stabilize the crystal packing, as shown in Figure S3, the first two are formed through the H atoms attached to the oxygen of the water molecule bound to nickel with two oxygens of two nitrates, namely Ow1H1wA O4 and Ow1H1wB O14 and the last bond is formed between the oxygen of the hydroxyl function of the ligand and another oxygen of the nitrate O44 H44 O24. The donor-acceptor D...A distances are all less than 3 Å, and the D-H...A angles range from 161.0(0) to 178.0(4)°, indicating strong hydrogen bonding interactions see Table S3.

## Magnetic Analysis.

The $\chi_M T$ temperature dependences for the complexes $Ni^{II}Ln^{III}$ (Ln = Ce, Gd, Tb, Dy) are reported in Figure 4. The room temperature values are 1.90, 9.29, 12.75, and 14.33 $cm^3$ K $mol^{-1}$ for **2**, **3**, **4**, and **5** complexes, respectively. Such experimental values are in agreement with the theoretical expected values of 1.96, 9.03, 12.98, and 15.33 $cm^3$ K $mol^{-1}$ for a single paramagnetic Ni(II) centre in an octahedral environment where the orbital moment is largely quenched with S = 1 and g = 2.15],[48] which are associated with isolated ground multiplet states for Ce(III) ($^2F_{5/2}$, $g_J$ = 6/7), Gd(III) ($^8S_{7/2}$, g = 2.00), Tb(III) ($^7F_6$, $g_J$ = 3/2) and Dy(III) ($^6H_{15/2}$, $g_J$ = 4/3), respectively.[49] The thermal variation of the $\chi_M T$ product highlighted three distinct behaviours.

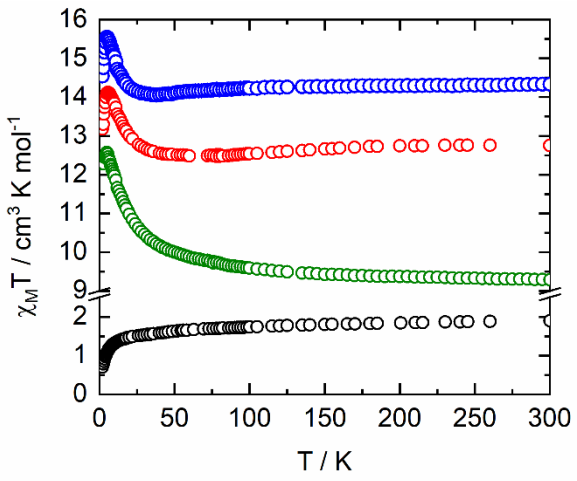


**Figure 4**. Thermal variation of the magnetic susceptibility $\chi_M T$ in the 2-300 K temperature range for complexes **2** (black), **3** (green), **4** (red), and **5** (blue).

For **2**, on cooling down to 2 K, the $\chi_M T$ values decrease monotonically to 0.70 $cm^3$ K $mol^{-1}$ due to the thermal depopulation of the $M_J$ states and possible dipolar antiferromagnetic interactions at very low temperature. For **3**, the $\chi_M T(T)$ curve slightly increased from room temperature to 100 K and then increased more rapidly until reaching a maximum of 12.57 $cm^3$ K $mol^{-1}$ at 5 K and finally slightly decreased at cryogenic temperature due to the zero-field splitting of the Ni(II). The increase of $\chi_M T$ and maximum value are in agreement with ferromagnetic interaction between the spin carriers and a total spin $S_T$ = 9/2 at 5 K. For both **4** and **5**, the $\chi_M T$ product slightly decreased due to the thermal depopulation of the $M_J$ states before increasing to reach maximum values of 14.12 $cm^3$ K $mol^{-1}$ at 6 K (for **4**) and 15.54 $cm^3$ K $mol^{-1}$ at 5 K (for **5**) because of ferromagnetic interaction between Ni(II) and Ln(III) ions. Below 5 K, the $\chi_M T$ value decreases are due to the combined magnetic anisotropy of Ni(II) and Ln(III). Such ferromagnetic interaction are often observed between paramagnetic Ni(II) and Ln(III) in literature[50-55] favouring the observation of slow magnetic relaxation.

Figure S4 depicted the field dependences of the magnetization measured at 2 K. The values reached under a magnetic field of 50 kOe are 2.00, 8.97, 7.32, and 6.33 Nβ for **2**, **3**, **4**, and **5** complexes, respectively. These values are in line with the expected saturation value for an isotropic Gd(III) ion and one Ni(II) ion, but far from the expected values when the Ni(II) is associated with a lanthanide ion, indicating significant magnetic anisotropy.

Given the DC magnetic properties, the three **2**, **4,** and **5** derivatives were investigated by ac magnetic measurements. None of these heterobimetallic systems exhibited an out-of-phase component ($\chi_M$'') of the magnetic susceptibility in zero applied field at 2 K (Figures S5-7). Such a lack of slow magnetic relaxation is often associated with the fast relaxation through efficient Quantum Tunnelling of the Magnetization (QTM), which could be overcome by applying an external dc field. In this way, the field dependence of the magnetic susceptibility of the three derivatives was investigated (Figures S5, S6, S8, and 5). The application of a DC field revealed a frequency dependence in the magnetic susceptibility. In case of **2**, the maxima of the $\chi_M$'' are localised at too high frequency (about 10 kHz) to allow a pertinent extraction of the relaxation and further ac thermal dependence study of the magnetic susceptibility (Figure S5). For both **4** and **5** compounds, an extended Debye model (Eq. SM1) was used to extract the relaxation time ($\tau$) at any dc field (Figures S6c and 5b, Table S4 and S5).[56-58] The resulting field dependence of the extracted $\tau$ showed that increasing the applied dc field value from 0 to 3000 Oe induced a slowing down of the relaxation time of the magnetization. The $\tau$ vs H curve for **5** could be fitted by Equation 1:

$$\tau^{-1}(T,H) = AH^4T + \frac{B_1}{1+B_2H^2} + \underbrace{\tau_0{}^{-1}\,\mathrm{e}\left(\frac{U_{\mathrm{eff}}}{k_{\mathrm{B}}T}\right) + CT^n}_{k(T)} \qquad \text{q. 1}$$

From left to right, the terms are the expressions of direct contribution (with A is a constant for the direct process, H the

magnetic field, and T the temperature), QTM contribution (with $B_1$ and $B_2$ as constants for the QTM process) and thermally activated contributions (Orbach and Raman processes, with $U_{eff}$ = effective energy barrier, $k_B$ the Boltzmann constant, C and n are respectively the constant and exponent for Raman process).

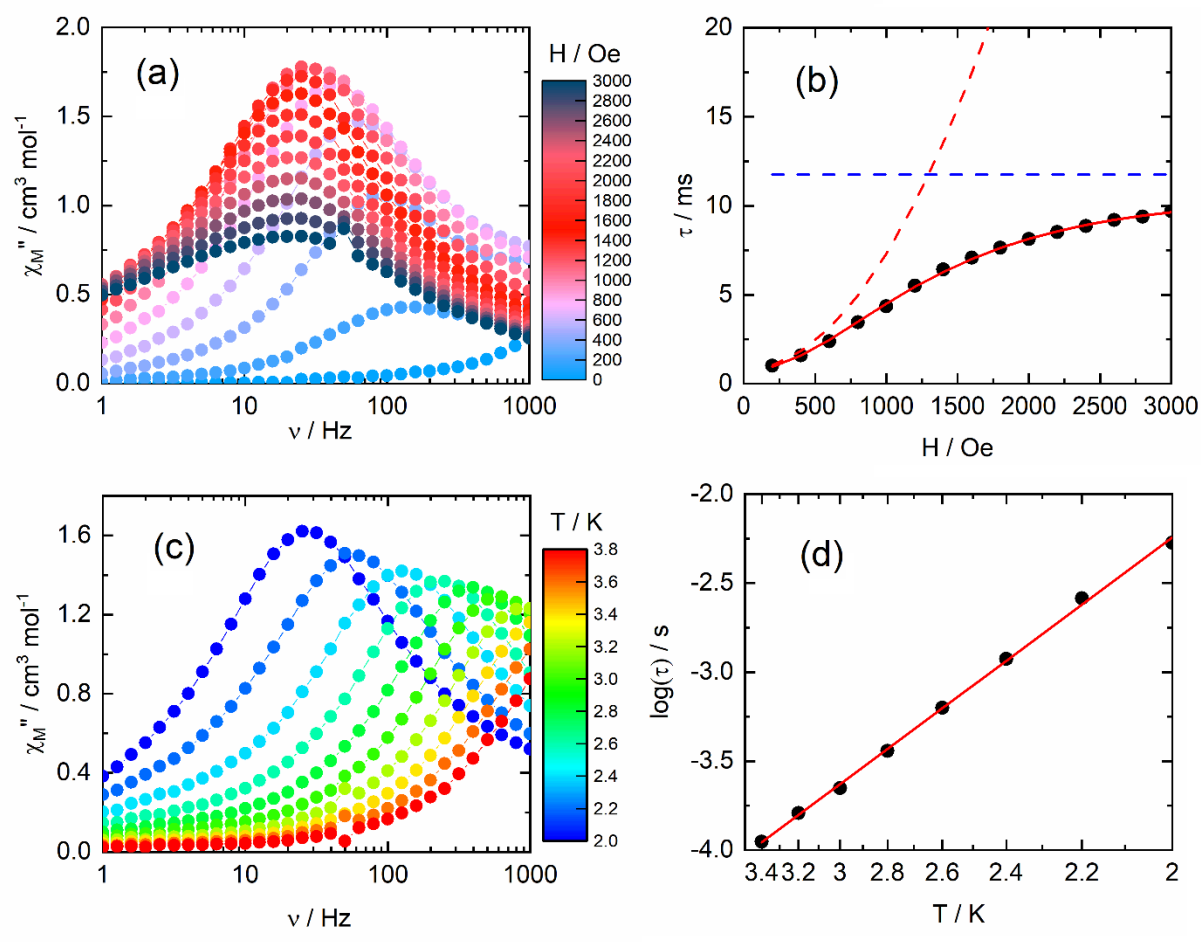


**Figure 5** . (a) Field dependence of the out-of-phase component of magnetic susceptibility ($\chi_M$'') at 2 K in the field range of 0–3000 Oe for **(5)**. (b) Field variation of the relaxation time (τ, black dots) for **(5)** with the best fitted curve in red. Red and blue dashed lines represent the QTM and thermally activated k(T) contribution (Orbach + Raman), respectively. Parameters are given in the text. (c) Frequency dependence of $\chi_M$'' at 1200 Oe in the temperature range of 2–3.8 K for **(5)**. (d) Temperature variations of the relaxation times in the range of 2 K to 3.4 K under 1200 Oe (full black circles). The red lines depict the best fits with parameters given in the text.

k(T) means that both Raman and Orbach processes are thermally dependent. The best fit was obtained with the following parameters: $B_1 = 1.29(13) \times 10^3$ $s^{-1}$, $B_2 = 8.41(11) \times 10^{-6}$ $Oe^{-2}$, $A = 1.17(11) \times 10^{-14}$ $s^{-1}$ $K^{-1}$ $Oe^{-4}$ and $k(T) = 1.18(5) \times 10^{-4}$ $s^{-1}$ (Figure 5b). 1400 Oe and 1200 Oe field values were selected as a good compromise between the $\chi_M$'' amplitude and the relaxation time (τ) to study the temperature-dependent behaviour of magnetic susceptibility for **4** and **5**, respectively (Figures 5c and S7). In such applied magnetic field, a frequency dependence of the magnetic susceptibility was observed for both compounds. Nevertheless, the multi-contribution character and the large shape of $\chi_M$'' did not permit a quantitative analysis. On the contrary, for **5**, τ was extracted using the extended Debye model (Eq. S1 and Table S6), and the resulting thermal variation of log(τ) is depicted in Figure 5d. The latter could be fitted using an Orbach process only with parameters $\Delta = 19.1(3)$ K and $\tau_0 = 3.99(4) \times 10^{-7}$ s. The normalized Argand attested that 85 % of the sample was involved in slow magnetic relaxation under an applied dc field of 1200 Oe (Figure S10). The nature of the magnetic relaxation process as well as the energy barrier value are in agreement with what was reported in literature for 3d4f heterobimetallic compounds.[59]

**Computational investigation**

**Description of the theoretical model and DFT geometry optimization**

Molecular geometries of the $Ni^{II}Ln^{III}$ systems were optimized at the ZORA/BP86/TZP level without symmetry constraint, but maintaining the $[Ni(\mu\text{-}O)_2Ln]$ crystal core geometry fixed. Indeed, it is necessary to proceed this way as the computed J exchange coupling value is very sensitive to the magnetic core geometry. Experimentally, the observed magnetic behavior by susceptibility measurements of the $Ni^{II}Ln^{III}$ systems reveals that the $Ni^{II}$–$Ce^{III}$ exchange carrier spins are antiferromagnetically coupled, while the $Ni^{II}$–$Ln^{III}$ (Ln = Gd, Tb, and Dy) congeners exhibit a Ferro exchange coupling. Therefore, the two hybrid B3LYP and PBE0 methods combined with the Broken Symmetry (BS) approach (see computational details) were used to rationalize the observed magnetic properties of the

$Ni^{II}Ln^{III}$ (Ln = Ce, Gd, Tb, Dy) complexes. We already showed that the used DFT/BS approach can be successfully applied in the case of transition and f-metal complexes,[60, 61] to predict satisfactorily the Ferro vs. AF coupling between two spin centers connected by the bridging spacer dioxo $(\mu\text{-}O)_2$ ligand. This approach also provided computed J exchange coupling constants in good agreement with the experimental data.[62] Two possible electron configurations of the $3d^8\text{-}4f^n$ of the considered $Ni^{II}Ln^{III}$ complexes (n = 1,7,8,9 for $Ce^{III}$, $Gd^{III}$, $Tb^{III}$, $Dy^{III}$, respectively) were considered for each complex, i.e., the $d^{2\alpha}\text{-}f^{n\alpha}$ High-Spin (HS) and the $d^{2\beta}\text{-}f^{n\alpha}$ Broken Symmetry (BS) states. In the HS state, the quartet ($S = \frac{3}{2}$) state is considered for the $Ni^{II}Ce^{III}$ ($d^{2\alpha}\text{-}f^{\alpha}$) species, while the *tentet* ($S = \frac{9}{2}$) spin state is considered for the $Ni^{II}Gd^{III}$ ($d^{2\alpha}\text{-}f^{7\alpha}$) congener. In the case of the $Ni^{II}Tb^{III}$ ($d^{2\alpha}\text{-}f^{6\alpha}$) and $Ni^{II}Dy^{III}$ ($d^{2\alpha}\text{-}f^{5\alpha}$) species, the *quintet* (S = 4) and *octet* ($S = \frac{7}{2}$) states are considered, respectively. Considering the BS state, the spin-flip recipe was applied, leading to the spin states ($M_S = 1$) state for the $Ni^{II}Ce^{III}$ ($d^{2\alpha}\text{–}f^{\beta}$) species, ($M_S = \frac{5}{2}$) spin state for the $Ni^{II}Gd^{III}$ ($d^{2\beta}\text{–}f^{7\alpha}$) system. For the $Ni^{II}Tb^{III}$ ($d^{2\beta}\text{–}f^{6\alpha}$) and $Ni^{II}Dy^{III}$ ($d^{2\beta}\text{–}f^{5\alpha}$) species, the spin states are respectively ($M_S = 2$) and ($M_S = \frac{3}{2}$). Apart from the number of structural differences that are expected to affect the magnetic coupling between the two $Ni^{II}$ and $Ln^{II}$ metal atoms within the $[Ni(\mu\text{-}O_b)_2Ln]$ core, the bridged Ni–$O_b$ and Ln–$O_b$ distances, Ni–$O_b$–Ln angles, and the Ni–O–Ln–O dihedral angle, are determining.

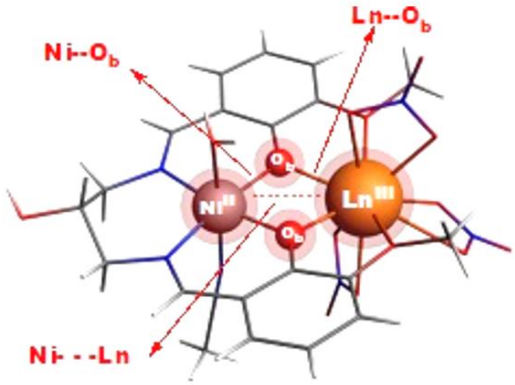


**Figure 6**: Structure of the $[Ni(\mu\text{-}O_b)_2Ln]$ core

The computed ZORA/BP86 relevant X-ray bond distances and angles parameters of the $[Ni(\mu\text{-}O)_2Ln]$ fixed core are displayed on Figure 6 and reported in Table 1. The optimized molecular geometry of the $Ni^{II}Ln^{III}$ complexes in their HS states is depicted on Figure 7. As can be seen in Table 1, there is a good agreement between the DFT/BP86/TZP optimized $[Ni(\mu\text{-}O)_2Ln]$ core structure and the X-ray data, reminding that the geometry of the magnetic core was kept fixed as it is in the crystal structure. The computed Ln–$O_b$ bond lengths and $Ni^{II}\cdots Ln^{III}$ distances decrease in the order Ce > Gd > Tb > Dy, in agreement with the lanthanide ionic radius contraction.[63] It is worth noting that the $[Ni(\mu\text{-}O)_2Ln]$ core moiety is quasi-planar, with a dihedral angle Ni-O-O-Ln of 9.9° *vs ca* 7.5° for $Ni^{II}$-$Ce^{III}$ and $Ni^{II}$-$Ln^{III}$ (Ln = Gd, Tb, Dy), respectively. As previous studies state,[60,61] this feature favors π-type bonding interaction leading to a $Ni^{II}\cdots Ln^{III}$ magnetic super-exchange through the dioxo-bridged $(\mu\text{-}O)_2$ path-linker. We also expect that the quasi-planar geometry of the $[Ni^{II}(\mu\text{-}O)_2Ln^{III}]$ asymmetric core could play a key role in magnetic superexchange interactions cooperatively with the covalently linked $Ni^{II}$–$(\mu\text{-}O)_2$–$Ln^{III}$ dioxo-bridged system. The electronic structure analysis will support this point.

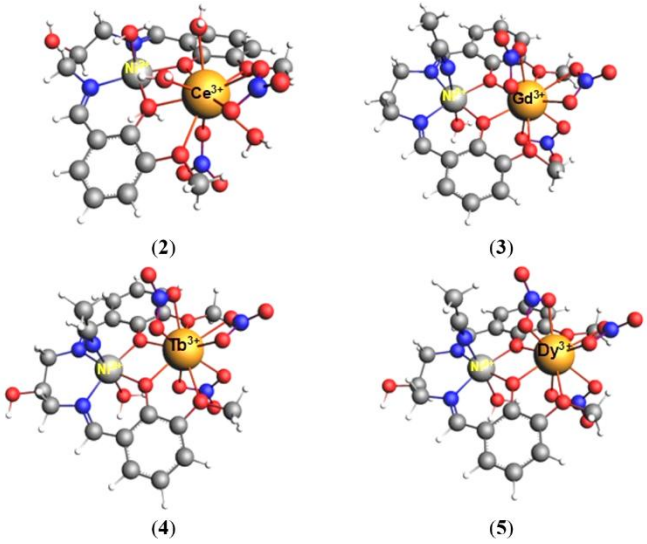


**Figure 7**: ZORA/BP86 optimized molecular structures of the $Ni^{II}Ln^{III}$ (Ln = Ce, Gd, Tb, Dy) complexes (oxygen atoms in red, nitrogen in blue, carbons in grey and hydrogens in white).

**Table 1**. Most relevant ZORA/BP86/TZP computed bond (Å) distances and angles (°) with the X-ray fixed $[Ni(\mu\text{-}O)_2Ln]$ core of the $Ni^{II}Ln^{III}$ (Ln = Ce, Gd, Tb, Dy) complexes in their HS states. X-ray data in bold.

| $Ni^{II}$-$Ln^{III}$ HS state | $Ni^{II}$-$Ce^{III}$ ($S_{max} = \frac{3}{2}$) | $Ni^{II}$-$Gd^{III}$ ($S_{max} = \frac{9}{2}$) | $Ni^{II}$-$Tb^{III}$ ($S_{max} = 4$) | $Ni^{II}$-$Dy^{III}$ ($S_{max} = \frac{7}{2}$) |
|---|---|---|---|---|
| Ni–$O_b$ | 2.022, 2.038 **2.022(7), 2.038(6)** | 2.015, 2.033 **2.015(2), 2.039(2)** | 2.014, 2.028 | 2.013, 2.028 |
| Ni–N | 2.019, 2.020 | 2.027, 2.040 | 2.037, 2.043 | 2.037, 2.041 |
| Ln-$O_b$ | 2.401, 2.437 | 2.327, 2.340 | 2.308, 2.326 | 2.294, 2.316 |
| Ni···Ln | 3.551 **3.550(2)** | 3.516 **3.516(5)** | 3.501 | 3.490 |
| <Ni-$O_b$-Ln> | 105.6 **105.2(2), 106.0(2)°** | 107.3 | 107.4 | 107.45 |
| $O_b$-Ni-$O_b$ $O_b$-Ln-$O_b$ | 81.0 66.0 | 78.1 66.2 | 77.8 66.4 | 77.6 66.6 |
| $Ni(\mu\text{-}O)_2Ln$ | 9.9 **9.7(2)°** | 7.5 | 7.9 | 7.1 |

**Electronic structure analyses**

To study in-depth the electronic structures and the nature of the metal-ligand bonding in the $Ni^{II}Ln^{III}$ complexes, natural population analyses (NPA),[64] Mayer,[65] and Nalewajski-Mrozek (NM) [66,67] bond order (BO) analyses were performed at the

ZORA/B3LYP and PBE0 level of theory. We focus on the [$Ni^{II}(\mu^2\text{-}O_b)Ln^{III}$] magnetic core (Figure 6) for the considered HS and BS states (*supra*).

The ZORA/B3LYP/TZP NPA atomic spin density ρ ($\rho_\alpha-\rho_\beta$), and computed net natural atomic charges (q), Mayer and NM bond orders are given in Table 2.

**Table 2**. ZORA/B3LYP/TZP NPA atomic spin density ρ ($\rho_\alpha-\rho_\beta$) and net charges (q), Mayer and NM average <Ni–$O_b$> and <Ln–$O_b$> bond orders of the $Ni^{II}Ln^{III}$ complexes in their HS and BS states.

| $Ni^{II}Ln^{III}$ | NPA Ni/$O_b$/Ln | | Bond Order <Ni–$O_b$> | | Bond Order <Ln–$O_b$> | |
|---|---|---|---|---|---|---|
| | ρ | q | Mayer | NM | Mayer | NM |
| $Ni^{II}Ce^{III}$ | | | | | | |
| ($S_{max} = 5/2$) HS | 1.60/0.05/1.00 | 1.38/–0.86/1.94 | 0.284 | 0.386 | 0.218 | 0.620 |
| ( $Ms$= 1) BS | 1.60/0.05/–1.00 | 1.38/–0.86/1.94 | 0.283 | 0.385 | 0.218 | 0.638 |
| $Ni^{II}Gd^{III}$ | | | | | | |
| ($S_{max}$= 9/2) HS | 1.60/0.06/6.99 | 1.39/–0.83/1.97 | 0.269 | 0.387 | 0.171 | 0.444 |
| ($Ms = 5/2$) BS | –1.60//–0.06/6.99 | 1.39/–0.83/1.97 | 0.268 | 0.383 | 0.170 | 0.449 |
| $Ni^{II}Tb^{III}$ | | | | | | |
| ($S_{max}$ = 4) HS | 1.61/0.06/5.98 | 1.42/–0.84/1.99 | 0.264 | 0.385 | 0.169 | 0.240 |
| ($Ms$ = 2) BS | –1.61/–0.05/5.98 | 1.42/–0.83/1.98 | 0.263 | 0.386 | 0.169 | 0.244 |
| $Ni^{II}Dy^{III}$ | | | | | | |
| ($S_{max}$ = 7/2) HS | 1.61/0.06/4.97 | 1.42/–0.83/1.97 | 0.258 | 0.384 | 0.180 | 0.284 |
| ( $Ms$ = 3/2) BS | –1.61/–0.05/4.97 | 1.42/–0.83/1.97 | 0.257 | 0.381 | 0.179 | 0.287 |

Interestingly, Table 2 shows that the atomic spin densities ρ of the magnetic metallic centers are close to the number of unpaired electrons of the $Ce^{III}$ ($f^1$), $Gd^{III}$ ($f^7$), $Tb^{III}$ ($f^8$), and $Dy^{III}$ ($f^9$) ions, *i.e.*, 1.0, 6.99, 5.98, and 4.97, respectively. In contrast, the value ($\rho = 1.6$) for the $Ni^{II}$ ($d^8$) is significantly lower than 2. These results are indicative of the spin delocalization (oxidation) and spin polarization, occurring for the transition metal ($Ni^{II}$) vs. lanthanide ($Ln^{III}$) ions, respectively, which will be discussed below.

It is noteworthy that the computed NPA charges on the metallic ions are significantly smaller than the formal value for $Ni^{II}$ (*ca*. +1.4) and $Ln^{III}$ (*ca*. +1.97), revealing the important ligand-to-metal donation. Moreover, the net charges (q) do not differ when passing from the HS to the BS states; as expected, the atomic spin densities (ρ) of the Ni ion exhibit an opposite sign in the BS state compared to the HS state. One can note that the $(\mu^2\text{-}O_b)_2$ bridged-dioxo spin populations (ca. 0.05e) are significantly lower than the unit, which could indicate a weak magnetic exchange coupling between the two metal centers in such complexes.

Moreover, the Mayer and NM <Ln–$O_b$> HS bond orders, the latter BO accounting for covalent and ionic interactions, are computed significantly greater for the $Ni^{II}Ce^{III}$ species (0.218 *vs*. 0.620) than for the Ferro $Ni^{II}Ln^{III}$ species (e.g., 0.169 *vs*. 0.244 for $Ni^{II}Tb^{III}$). Moreover, the Mayer <Ni–$O_b$> values are slightly greater for $Ni^{II}Ce^{III}$ species. These results correlate with the higher polarization effects and covalency (delocalization) in the <Ln–$O_b$> bonding within the AF $Ni^{II}Ce^{III}$ system than in the Ferro $Ni^{II}Ln^{III}$ congeners, and will be assessed by orbital analysis below.

**DFT evaluation of the exchange coupling constant J:**

The literature on computed coupling constants J for the 3d–4f binuclear complexes is particularly scarce.[68a-c] The rigorous computations of the exchange coupling constant J, would be to employ highly correlated *ab initio* methods such as CASSCF and CASPT2 or DDCI (difference dedicated CI) methods. These latter methods are developed to obtain accurate energy differences between spin states.[68d] However, such calculations are very time-consuming and are limited to small systems or to models mimicking actual structures. For our part, we investigated computationally the magnetic character of the $Ni^{II}Ln^{III}$ complexes at the scalar relativistic ZORA level employing the two B3LYP and PBE0 functionals. We remind that the $Ni^{II}Ce^{III}$ complex exhibits experimentally an AF character within the [$Ni^{III}(\mu\text{-}O)_2Ce^{III}$] core, whereas their $Ni^{II}Ln^{III}$ (Ln = Gd, Tb, Dy) congeners exhibit Ferro exchange interactions. As aforementioned, we make use of the Yamaguchi formula in combination with the BS approach to estimate the $Ni^{II}$—$Ln^{III}$ coupling constant J ($cm^{-1}$) (see computational details). Regarding the magneto-structural properties of such [$Ni^{III}(\mu\text{-}O)_2Ln^{III}$] dioxo-bridged complexes, the exchange coupling constant J($cm^{-1}$) depends strongly on several structural factors: the Ni–$O_b$ and Ln–$O_b$ distances and the Ni–$O_b$–Ln angle. We remind that the geometry of the $Ni^{II}Ln^{III}$ complexes has been optimized keeping fixed the crystal geometry of the [$Ni^{III}(\mu\text{-}O)_2Ln^{III}$] magnetic core.

**Table 3**: ZORA/B3LYP computed TBE(eV) for HS/BS states (in eV), ΔE($cm^{-1}$) energy differences, HS and BS <$S^2$> values, and exchange coupling J($cm^{-1}$) constant.

[a] [59, 68-70]

| $Ni^{II}Ln^{III}$ (eV) | HS | BS | $\Delta(cm^{-1})$ | $\langle S^2 \rangle$ (exact) | | $J_{Ni\text{-}Ln}$ ($cm^{-1}$) | |
|---|---|---|---|---|---|---|---|
| | | | | | | T | fit |
| | | | | | | 82 | - |
| | | | | | | 03 | +0.7/+3.6[a] |
| | | | | | | 44 | - |
| | | | | | | 35 | - |

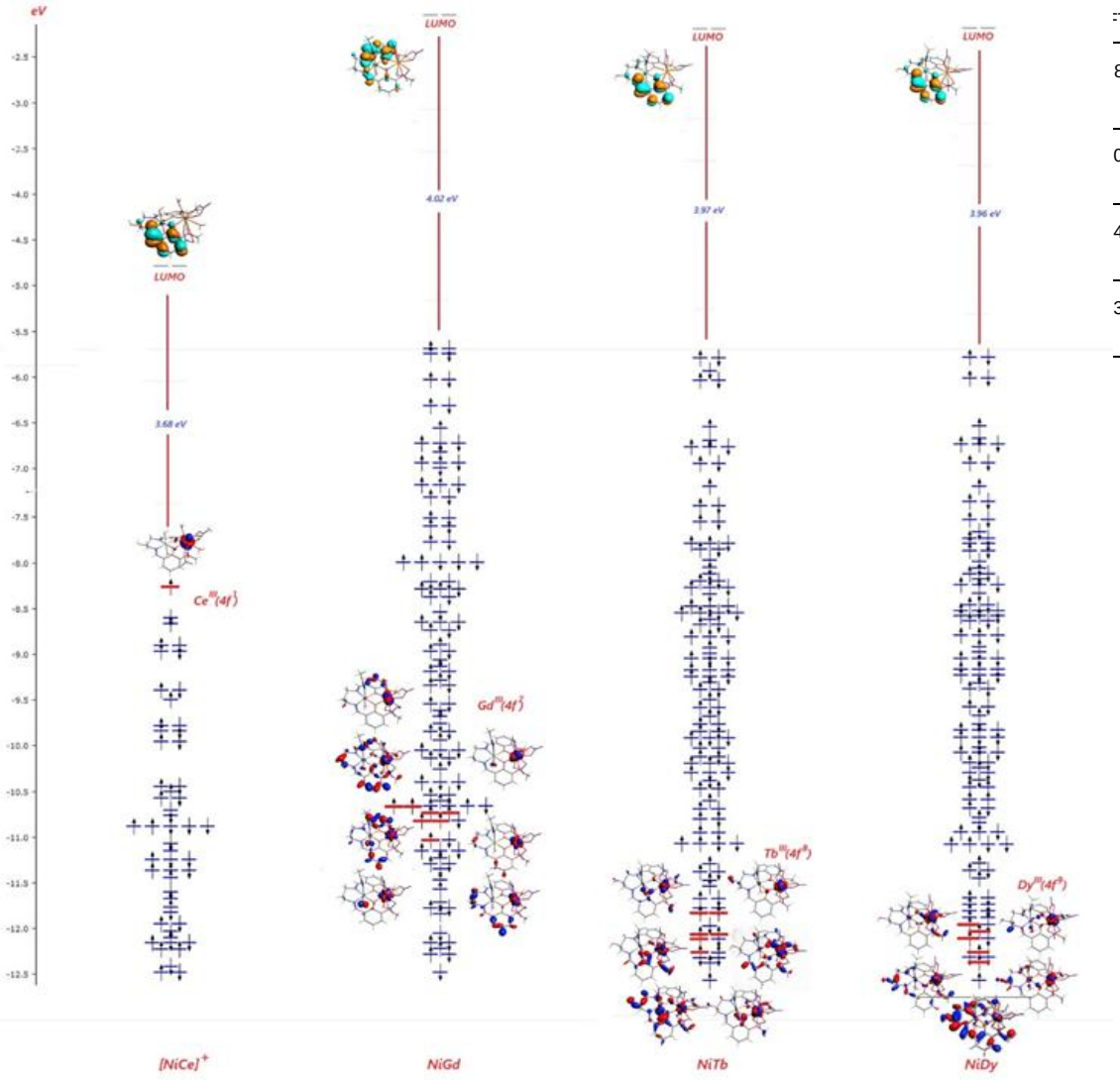


**Figure 8**: ZORA/B3LYP $\alpha$ HS spin-orbital diagrams of the $Ni^{II}Ln^{III}$ (Ln = Ce, Gd, Tb, Dy) complexes

In Table 3, the computed ZORA/B3LYP Total Bonding Energy TBE(eV), $\Delta E = E_{BS} - E_{HS}$ energy differences, the mean values $\langle S^2 \rangle$ of the squared spin operator through which spin contamination of the HS state can be estimated, as well as the computed exchange coupling J($cm^{-1}$) constants are reported. The ZORA/PBE0 data are reported in supplementary information (Table S7).

We can note that the computed $\langle S^2 \rangle$ exhibits correct values for all HS $Ni^{II}Ln^{III}$ (Ln = Ce, Gd, Tb, Dy) states. Indeed, the computed S(S+1) values are close to the exact ones for the $Ni^{II}Ce^{III}$ quartet ($S_{max} = \frac{3}{2}$) state, the $Ni^{II}Gd^{III}$ tentet ($S_{max} = \frac{9}{2}$) state, the $Ni^{II}Tb^{III}$ nonet ($S_{max} = 4$) state, and the $Ni^{II}Dy^{III}$ octet ($S_{max} = \frac{7}{2}$) state. These results indicate no spin contamination for the HS states. Furthermore, as expected, the computed $\langle S^2 \rangle$ values for the BS state, are intermediate between the exact low spin state values and HS ones, e.g., for the $Ni^{II}Ce^{III}$ state, the computed BS value (S = 1.75) is between the doublet (S = 0.75) state and the quartet S(S+1) = 3.75 HS state. An important observation from the results in Table 3 is that the observed AF coupling within the $[Ni^{II}(\mu\text{-}O)_2Ce^{III}]$ core is correctly predicted. More interestingly, the computed exchange coupling constants J($cm^{-1}$) (Table 3) agree well with the reported experimental magnetic data,[59] and with previous computational and experimental results in the case of NiGd species.[59,69,70] Indeed, the computed exchange coupling constant (J = +1.03 $cm^{-1}$) for the $Ni^{II}Gd^{III}$ system, agrees well with the reported most similar heterobimetallic dioxo-bridged $[Ni(\mu^2\text{-}O)Gd^{III}]$ core *i.e.*, the $[LNi^{II}Gd(EtOH)_2](EtOH)_2$ and $[LNi^{II}(H_2O)_2Gd](NO_3)_3$ (L = [2,2-[2,2-Dimethyl-1,3-propanediylbis(nitrilomethylidyne)]bis(6-methoxyphenolato)(2-)]) complexes. These species exhibit fitted Ferro J constant of +3.6 and +0.7 $cm^{-1}$, respectively [68-70]. Moreover, DFT computations leading to Ferro exchange coupling ($J_{Ni\text{-}Gd}$ = +1.78 and +2.11 $cm^{-1}$) in $Ni^{II}Gd^{III}$ systems were reported,[59, 68b] which agree well with our findings, and offer confidence in the computed J values.

**MO analysis**

Historically, the theoretical orbital interpretation of superexchange interactions has been developed using the Hay-Thibeault-Hoffmann model,[71] which indicates that the bridging overlap interactions between the ligand atomic orbitals and the metal d orbitals determine the sign and magnitude of the magnetic coupling constant between the metal centers. Recently, McAdams et al.[72] in their report on the magnetic exchange of f-elements with 3d metals, highlighted that the enhanced covalency in dioxo-bridged M-(μ-O)-M framework favors magnetic superexchange. Kohn-Sham orbitals are well suited for qualitatively analyzing magnetic exchange, offering valuable insights.[68] The comparative spin-unrestricted α-MO diagrams of the $Ni^{II}Ln^{III}$ (Ln = Ce, Gd, Tb, Dy) systems in their HS states are shown on Figure 8. One can note in these diagrams that the highest SOMOs of the $Ni^{II}Ln^{III}$ (Ln = Gd, Tb, Dy) systems are composed of NiL and $NO_3$ contributions. In opposite, for the $Ni^{II}Ce^{III}$ congener, the electronic structure exhibits the highest SOMO with pure $4f^1$ metallic orbitals. In the cases of $Ni^{II}Gd^{III}$, $Ni^{II}Tb^{III}$, and $Ni^{II}Dy^{III}$ species, the contracted $4f^n$ levels are computed at deeper energies due to the efficient shielding of the 5s and 5p occupied subshells.[68] Notably, as shown by their isodensity surfaces, the spin orbitals displaying the $4f^n$ metallic electrons in $Ni^{II}Ln^{III}$ (Ln = Gd, Tb, Dy) are partially delocalised relatively to the more localised SOMO ($4f^1$) of the $Ni^{II}Ce^{III}$ system.

**Spin densities analysis.**

It is established that spin density mapping in HS and BS states plays a key role in the qualitative understanding of the magnetic exchange coupling.[70,73] As aforementioned, in the magneto-chemistry of d-transition complexes,[60,62] spin polarization and spin delocalization phenomena were proposed in the early 1990s by O. Kahn et al.[59, 74] to explain the exchange or super-exchange coupling between the magnetic centers. Thus, the obtained ZORA/B3LYP/TZP spin density surfaces (difference between α and β electron densities) for the considered complexes are displayed on Figure 9 for the HS and BS states.

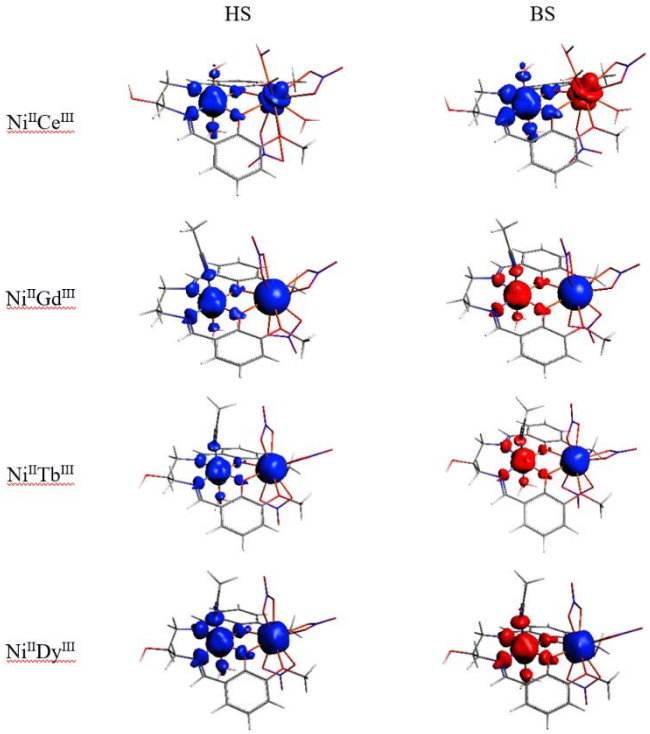


**Figure 9**: ZORA/B3LYP/TZP spin density surfaces for the HS and BS states of the $Ni^{II}Ln^{III}$ (Ln = Ce, Gd, Tb, Dy) complexes (blue color: positive and red color: negative spin density). The plotted isodensity surfaces correspond to a value of 0.0025 e $bohr^{-3}$.

We can note on Figure 9, that both HS and BS spin densities are mainly localized on the two magnetic $Ni^{II}$ and $Ln^{III}$ centers with non-negligible contributions from the $(\mu^2\text{-}O_b)_2$ bridged-dioxo atoms and the N-ligand neighbors. In the HS state, the two bridging oxygen atoms and two nitrogen atoms coordinated to the $Ni^{II}$ exhibit positive spin densities due to delocalization mechanisms. On the contrary, for the BS state, the two oxygen atoms are differently polarized with negative sign of spin densities due to the polarization effect of Ln ions. In the case of the $Ni^{II}Ce^{III}$ system, the $Ce^{III}$ ion is β spin-flipped, leading to positive spin on bridged atoms. One can note that the spin density map differs from the NiCe species to the $Ni^{II}Ln^{III}$ (Ln = Gd, Tb, Dy) congeners, in particular, the isosurface of the $Ce^{III}$ ion can be identified as the $4f_z^2$ orbital, correlating well with the pure 4f metallic SOMO of the complex. Moreover, the isosurfaces of the $Gd^{III}$, $Tb^{III}$, and $Dy^{III}$ ions are mostly spherical due to the high mixing of several 4f orbitals.

## Conclusion

Four Schiff base complexes LNiLn (Ln = Ce (**2**), Gd (**3**), Tb (**4**), and Dy (**5**), $H_2L$ = N, N'-bis(3-methoxysalicylaldiimine)-1,3-propylene-2-ol) were synthesized. Single crystal X-ray diffraction demonstrated that compound **2** crystallizes in the tetragonal system while the other three **3**, **4**, and **5** congeners crystallize in the monoclinic system. Nevertheless they are all 3d4f hetero-bimetallic dinuclear complexes in which the Ni(II) and Ln(III) ions are localised in the N2O2 and O4 coordination pockets, respectively. Static magnetic measurements demonstrated ferromagnetic interaction between the paramagnetic Ni(II) and the trivalent lanthanide for the three compound **3**-**5** (Ln = Gd, Tb and Dy) while such interaction could not be evidenced in case of Ce(III). At 2 K, ac magnetic measurements highlighted a field-induced SMM behavior for the four heterobimetallic systems. Moreover, for **5**, the linear dependence of log(τ) suggested that the main relaxation process of the magnetization is Orbach with $\Delta$ = 19.1(3) K and $\tau_0$ = 3.99(4) × $10^{-7}$ s. The ZORA/B3LYP computations satisfactorily predict the AF *vs* Ferro character for the $Ni^{II}\ldots Ce^{III}$ exchange coupling *vs* the $Ni^{II}\ldots Ln^{III}$ (Ln = Gd, Tb, Dy) congeners, providing exchange coupling constants of J = –2.82, +1.03, +5.44, and +1.35 $cm^{-1}$, in agreement with experimental trends. The low magnitude of the magnetic exchange coupling is mainly due to the low spin polarization along the dioxo-bridge linking the two metallic $Ni^{II}$ et $Ln^{III}$ spin carriers. Moreover, the Mayer and NM <Ln–$O_b$> HS bond orders are computed significantly greater for the $Ni^{II}Ce^{III}$ species than for the Ferro $Ni^{II}Ln^{III}$ species (Ln = Gd, Tb, Dy), thus favoring the AF superexchange in the former species.

## Experimental Section

**Synthesis. General Procedures and Materials.**

The starting nickel complex (**1**) was prepared according to an experimental procedure previously described.[36] All starting materials, including orthovanillin, 1,3-diaminopropan-2-ol, triethylamine, nickel(II) nitrate hexahydrate, cerium(III) nitrate hexahydrate, gadolinium(III) nitrate hexahydrate, terbium(III) nitrate pentahydrate, and dysprosium(III) nitrate, as well as solvents like ethanol, tetrahydrofuran, and acetonitrile, were acquired from Sigma-Aldrich at reagent grade purity and utilized without additional purification. A Perkin-Elmer 240 C elemental analyzer was used for C, H, and N analysis. IR spectra (4000–400 $cm^{-1}$) were recorded as KBr pellets on a Perkin Elmer (spectrum two) FT-IR spectrophotometer. A Lambda 25 Perkin Elmer UV-Vis spectrometer was employed to measure complex absorbance.

**Synthesis**

**$[LNi(H_2O)_2Ce(H_2O)_3(NO_3)_2](NO_3)$ (2)**. To a solution of complex (**1**) (0.178 mmol, 0.08 g) in 20 mL of a 50:50 methanol/ethanol mixture, a solution of $Ce(NO_3)_3{\cdot}6H_2O$ (0.191 mmol, 0.083 g) in 10 mL of the same solvent mixture was added. The resulting mixture was stirred for 30 minutes at room temperature, yielding a green solution. Green crystals suitable for X-ray diffraction analysis formed over few weeks through slow solvent evaporation. The yield of the reaction was 90%. IR (KBr, $cm^{-1}$): 3369, 1630, 1466, 1296, 1036,742. UV (λ max, DMSO): 268.07 nm and 353.77 nm (see figure S1).
**$[LNi(H_2O)(CH_3CN)Gd(NO_3)_3]$ (3).** A solution of $Gd(NO_3)_3{\cdot}6H_2O$ (0.188 mmol, 0.085 g) in 10 mL of acetonitrile was combined with a solution of complex (**1**) (0.178 mmol, 0.08 g) in 20 mL of acetonitrile. The resulting mixture was stirred for 30 minutes at room temperature, producing a purple solution. Slow evaporation of the solvent yielded purple crystals suitable for X-ray diffraction analysis. The yield of the reaction was 75%. IR (KBr, $cm^{-1}$): 3566, 3488, 3434, 1631, 1414, 1223, 1036, 740. UV (λ max, DMSO): 267.54 nm and 353.55nm, see Figure S1.
**$[LNi(H_2O)(CH_3CN)Tb(NO_3)_3]$ (4) and $[LNi(H_2O)(CH_3CN)Dy(NO_3)_3]$ (5).** The synthesis of the complexes involving $Tb(NO_3)_3.5H_2O$ and $Dy(NO_3)_3.xH_2O$ followed the identical procedure outlined for complex **3**. The respective yields for these complexes were 77% and 72%.

**Crystallography**

Four suitable crystals were selected for single-crystal X-ray diffraction experiments: (colourless stick, dimensions = 0.320 x 0.080 x 0.070 mm) of **2**, (violet block, dimensions = 0.580 x 0.510 x 0.360 mm) of **3**, (colourless prism, dimensions = 0.140 x 0.220 x 0.300 mm) of **4**, (colourless plate, dimensions = 0.070 x 0.260 x 0.320 mm) of **5.** Crystals **2** and **3** are mounted on the goniometer head of a APEXII Kappa-CCD (Bruker. AXS) diffractometer equipped with a CCD-LDI-APEX2 detector, while the other two are mounted with a cryoloop on the goniometer head of a D8 Venture (Bruker-AXS) diffractometer equipped with a CMOS-PHOTON70 detector, using Mo-K_ radiation (λ=0.71073 Å, multilayer monochromator) at T = 150(2) K. Crystal structure was solved by dual-space algorithm using SHELXT program,[75] and then refined with full-matrix least-squares methods based on $F^2$ (SHELXL program[76]). The contribution of the disordered solvents to the calculated structure factors was estimated following the BYPASS algorithm,[77] implemented as the SQUEEZE option in PLATON.[78] A new data set, free of solvent contribution, was then used in the final refinement. All non-Hydrogen atoms were refined with anisotropic atomic displacement parameters. Except for the hydrogen atoms of the water molecules that were introduced in the structural model with the help of the HYDROGEN software,[79] H atoms were finally included in their calculated positions and treated as riding on their parent atom with constrained thermal parameters. Molecular graphics were generated using the Diamond software package. A summary of the crystal data collection and refinement parameters is presented in Table S1. Deposition Numbers 2443680 (for **2**), 2443679 (for **3**) contain the supplementary crystallographic data for this paper. These data are provided free of charge by the joint Cambridge Crystallographic Data Centre and Fachin formations zen-trum Karlsruhe Access Structures service www.ccdc.cam.ac.uk/ structures.

**Magnetic Measurements**

The DC magnetic susceptibility measurements were performed on a solid immobilized polycrystalline sample with a Quantum Design MPMS magnetometer between 2 and 300 K in an applied magnetic field of 0.02 T for temperatures of 2-20 K, 0.2 T for temperature of 20-80 K and 1T for temperatures of 80-300 K. The *ac* magnetic susceptibility measurements were performed on Quantum Design MPMS magnetometers in the 1-1000 Hz frequency range and on Quantum Design PPMS magnetometers in the 50-10000 Hz frequency range. These measurements were all corrected for the diamagnetic contribution as calculated with Pascal's constants.

**Computational Details**

All calculations were performed with the Amsterdam Molecular Simulations AMS2024.102 release program with the Amsterdam Density Functional (ADF) engine.[80,81] Scalar relativistic corrections have been introduced via the zeroth-order regular approximation (ZORA).[82,83] In all cases, the starting molecular structures for the geometry optimizations are derived from the X-ray structures of the $[LNi^{II}Ln^{III}]^{+/0}$ (Ln = Ce, Gd, Tb, Dy; L = Schiff Base) complexes. As successfully used previously,[84,85] the geometry optimization of the $Ni^{II}Ln^{III}$ complexes was carried out keeping fixed the X-ray structure of the $[Ni(\mu\text{-}O_b)_2Ln]$ core. The Becke and Perdew (BP86) functional[86,87] was used to optimize the geometry of the High Spin (HS) states utilizing triple-ζ-plus polarization (TZP) all-electron Slater-type orbitals (STO) basis sets. Furthermore, two hybrid functional B3LYP[88-91] and PBE0[92,93] have been used to calculate the exchange coupling constant J. Using the BP86 optimized geometry, a single-point computation was performed to determine the B3LYP and PBE0 energies of the HS states. Then, using the spin-flip recipe included in the AMS/ADF program,[94] the Broken Symmetry (BS) states[95,96] were calculated using the MOs of the HS structures as an initial guess. ADF strict convergence criteria and integral precision were achieved by using the grid numerical quality of $10^{-6}$ eV (numerical accuracy keyword "good"). It is important to note that the ADF program computes Total Bonding Energies (TBE) rather than total energies; however, this distinction does not affect the energy differences relevant to the magnetic exchange coupling constants. In the framework of the BS approach,[95,96] the J constant is deduced from the energy difference between the HS and BS states according to the Heisenberg-Dirac-van Vleck (HDvV) Hamiltonian, which takes the form $\hat{H} = -J_{12}\,\hat{S}_1{\cdot}\hat{S}_2$, in the case of two spin centers. A positive J indicates ferromagnetic coupling (Ferro) and the negative sign an antiferromagnetic one (AF). The J constant is computed using the Yamaguchi formula[97-99]:

Yamaguchi formula is used: $J_{AB} = \frac{E_{BS}-E_{HS}}{<S^2>_{HS}-<S^2>_{BS}}$ (1)

In this formula, $<S^2>_{HS}$ and $<S^2>_{BS}$ are respectively the mean values of the squared spin operator for the HS and BS states. Molecular structure drawing, spin densities, and molecular orbital (MO) were plotted using the ADF-GUI auxiliary program.[80,81]

## Data Availability Statement

The data that support the findings of this study are available in the supplementary material of this article.

## Acknowledgements

The authors are grateful to the Frères Mentouri University of Constantine 1 (Algeria), University of Rennes, CNRS and the Pharmaceutical Sciences Research Center (CRSP) for providing computing facilities. The General Directorate of Scientific Research and Technological Development (DGRSDT) for the PRFU project (2022-2024: Grant No. B00L01EN250120220001) and the Thematic Research Agency in Health and Life Sciences – ATRSSV for the PNR (Grant 2022-2024) are also acknowledged.

**Keywords:** Schiff Base • 3d4f heterobimetallic • Single-Molecule Magnet • Exchange coupling • computational investigation • magneto-structural correlations

D. Gatteschi, R. Sessoli and J. Villain, Molecular Nanomagnets, Oxford University Press, 2006.

[2] R. A. Layfield, M.-L. Tong, B. M. Day, Y.-C. Chen, F.-S. Guo, A. Mansikkamaki, *Science*, **2018**, *362*, 1400–1403.

[3] M. Mannini, F. Pineider, P. Sainctavit, C. Danieli, E. Otero, C. Sciancalepore, A. M. Talarico, M.-A. Arrio, A. Cornia, D. Gatteschi, R. Sessoli, *Nat. Mater.* **2009**, *8*, 194–197.

[4] S. Thiele, F. Balestro, R. Ballou, S. Klyatskaya, M. Ruben, W. Wernsdorfer, *Science* **2014**, *344*, 1135–1138.

[5] K. S. Pedersen, A.-M. Ariciu, S. McAdams, H. Weihe, J. Bendix, F. Tuna, S. Piligkos, *J. Am. Chem. Soc.* **2016**, *138*, 5801–5804.

[6] H. Douib, B. Lefeuvre, K. Dhbaibi, J. Flores Gonzalez, V. Dorcet, F. Pointillart, *Chem. Asian. J.* **2025**, e202500234

[7] Y. N. Guo, G. F. Xu, W. Wernsdorfer, L. Ungur, Y. Guo, J. Tang, H.-J. Zhang, L. F. Chibotaru, A. K. Powell, *J. Am. Chem. Soc.* **2011**, *133*, 11948–11951

[8] R. Sessoli, A. K. Powell, *Coord. Chem. Rev.* **2009**, *253*, 2328–2341.

[9] T. N. Hooper, J. Schnack, S. Piligkos, M. Evangelesti, E. K. Brechin, *Angew. Chem., Int. Ed.* **2012**, *51*, 4633–4636.

[10] J. W. Sharples, D. Collison, *Coord. Chem. Rev.* **2014**, 260, 1–20.

[11] K. R. Vignesh, S. K. Langley, K. S. Murray, G. Rajaraman, *Chem. – Eur. J.* **2017**, *23*, 1654–1166.

[12] H. L. C. Feltham, S. Brooker, *Coord. Chem. Rev.* **2014**, *276*, 1–33.

[13] F. A. Mautner, F. Bierbaumer, R. C. Fischer , A. Tubau, S. Speed, E. Ruiz, S. S. Massoud, R. Vicente, S. Gomez-Coca, *Inorg. Chem.* **2022**, *61*, 11124-11136

[14] J. J. Le Roy, I. Korobkov, J. E. Kim, E. J. Schelter, M. Murugesu, *Dalton Trans.* **2014**, *43*, 2737−2740.

[15] H. Wada, S. Ooka, T. Yamamura, T. Kajiwara, *Inorg. Chem.* **2017**, *56*, 147−155.

[16] A. Upadhyay, K. R. Vignesh, C. Das, S. K. Singh, G. Rajaraman, M. Shanmugam, *Inorg. Chem.* **2017**, *56*, 14260−14276.

[17] M.-X. Xu, Y.-S. Meng, J. Xiong, B.-W. Wang, S.-D. Jiang, S. Gao, *Dalton Trans.* **2018**, *47*, 1966−1971.

[18] S. K. Gupta, S. Shanmugan, T. Rajeshkumar, A. Borah, M. Damjanović, M. Schulze, W. Wernsdorfer, G. Rajaraman, R. Murugavel, *Dalton Trans.* **2019**, *48*, 15928−15935.

[19] S. Hino, M. Maeda, K. Yamashita, Y. Kataoka, M. Nakano, T. Yamamura, H. Nojiri, M. Kofu, O. Yamamuro, T. Kajiwara, *Dalton Trans.* **2013**, *42*, 2683−2686.

[20] S. Hino, M. Maeda, Y. Kataoka, M. Nakano, T. Yamamura, T. Kajiwara, *Chem. Lett.* **2013**, *42*, 1276−1278.

[21] C. Takehara, P. L. Then, Y. Kataoka, M. Nakano, T. Yamamura, T. Kajiwara, *Dalton Trans.* **2015**, *44*, 18276−18283.

[22] Q.-W. Li, R.-C. Wan, Y.-C. Chen, J.-L. Liu, L.-F. Wang, J.-H. Jia, N. F. Chilton, M.-L. Tong, *Chem. Commun.* **2016**, *52*, 13365−13368.

[23] T. Shi, Y. Xu, M.-X. Li, C.-M. Liu, E. N. Nfor, Z.-X. Wang, *Polyhedron* **2020**, *188*, 114695.

[24] F. Pointillart, O. Cador, B. Le Guennic, L. Ouahab, *Coord. Chem. Rev.* **2017**, *346*, 150-175.

[25] A. Ben Khélifa, M. Salah Belkhiria, G. Huang, S. Freslon, O. Guillou, K. Bernot, *Dalton Trans.*. **2015**, *44*, 16458-16464.

[26] A. Vráblová, M. Tomás, L. R. Falvello, Ľ. Dlháň, J. Titiš, J. Černák, R. Boča, *Dalton Trans.* **2019**, *48*, 13943-13952.

[27] S. K. Singh, T. Gupta, L. Ungur, G. Rajaraman, *Chem. Eur. J.* **2015**, *21*, 13812-13819.

[28] E. Costa-Villén, M. Font-Bardia, J. Mayans, A. Escuer, C*ryst. Growth Des.* **2024**, *24*, 5806-5817.

[29] R. Koner, H. H. Lin, H. H. Wei, S. Mohanta, *Inorg. Chem*. **2005**, *44*, 3524-3536.

[30] H. R. Wen, S. J. Liu, X. R. Xie, J. Bao, C. M. Liu, J. L. Chen, *Inorg. Chimica Acta*. **2015**, *435*, 274-282.

[31] S. L. Zhang , D. Y. Ma, X. X Zhou, H. Q. Liu, Y. L. Wang, S. S. Li, *J.Mol. Struct*. **2024**, *1303*, 137637.

[32] N. Ahmed, C. Das, S. Vaidya, A. K. Srivastava, S. K. Langley, K. S. Murray, M. Shanmugam, *Dalton Trans*. **2014**, *43*, 17375-17384.

[33] J. P. Costes, S. Mallet-Ladeira, L. Vendier, R. Maurice, W. Wernsdorfer, *Dalton Trans*. **2019**, *48*, 3404-3414.

[34] J. P. Costes, L. Vendier, "Structural and magnetic studies of new $Ni^{II}$–$Ln^{III}$ complexes" *Wiley Online Library*. **2010**, *18*, 2768.

[35] B. Dutta, T. Guizouarn, F. Pointillart, K. Kotrle, R. Herchel, D. Ray, *Dalton Tran*s. **2023**, *52*, 10402-10414.

[36] T. D. Pasatoiu, J. P. Sutter, A. M. Madalan, F. Z. Chiboub Fellah, C. Duhayon, M. Andruh, *Inorg. Chem*. **2011**, *50*, 5890-5898.

[37] M. X. Yao, X. Y. Lu, Z. X. Zhu, X. W. Deng, S. Jing, *New J. Chem*. **2015**, *39*, 8356-8363.

[38] E. Colacio, J. Ruiz, A. J. Mota, M. A. Palacios, E. Cremades, E. Ruiz, F. J. White, E. K. Brechin, *Inorg. Chem*. **2012**, *51*, 5857-5868.

[39] J. P. Costes, F. Dahan, C. Duhayon, A. J. Mota, *Polyhedron.* **2015**, *96*, 51-56.

[40] S. Ghosh, A. Ghosh, *Inorg. Chim. Acta*. **2016**, 442, 64-69.

[41] F. Z. Chiboub Fellah, F. Pointillart, T. Guizouarn, T. Roisnel, N. Dege, A. Chiboub Fellah, R. Hassaine, *Eur. J. Inorg. Chem*. **2022**, 27, e202200349.

[42] F. Z. Chiboub Fellah, S. Boulefred, A. Chiboub Fellah, B. El Rez, C. Duhayon, J. P. Sutter, *Inorg. Chim. Acta*. **2016**, *439*, 24-29.

[43] F. Z. Chiboub Fellah, C. Duhayon, S. Mallet-Ladeira, L. Vendier, J. P. Costes, *Polyhedron*. **2022**, *224*, 116015.

[44] C. Linden, S. V. Eliseeva, N. Chaudhary, M. Zeller, S. Petoud, E. R. Trivedi, *Eur. J. Inorg. Chem*. **2020**, *1*, 75-78.

[45] K. Liu, W Shi, P. Cheng, *Coord. Chem. Rev*. **2015**, 289, 74-122.

[46] W. Y. Bi, X. Q. Lü, W. L. Chai, J. R. Song, W. K. Wong, X. P. Yang, R. A. Jones, *Z. für Anorg. Allg. Chem*. **2008**, 634, 1795-1800.

[47] L. Jiang, Y. Liu, X. Liu, J. Tian, S. Yan, *Dalton Trans.* **2017**, 46, 12558-12573.

[48] K. E. R. Marriott, L. Bhaskaran, C. Wilson, M. Medarde, S. T. Ochsenbein, S. Hill, M. Murrie, *Chem. Sci.* **2015**, 6, 6823-6828.

[49] O. Kahn, Molecular Magnetism, VCH, Weinhem, **1993**.

[50] C. Meseguer, S. Titos-Padilla, M. M. Hänninen, R. Navarrete, A. J. Mota, M. Evangelisti, J. Ruiz, E. Colacio, *Inorg. Chem.* **2014**, *53*, 12092–12099.

[51] M. Towatari, K. Nishi, T. Fujinami, N. Matsumoto, Y. Sunatsuki, M. Kojima, N. Mochida, T. Ishida, N. Re, J. Mrozinski, *Inorg. Chem.* **2013**, *52*, 6160–6178.

[52] A. Bhanja, E. Moreno-Pineda, R. Herchel, W. Wernsdorfer, D. Ray, *Dalton Trans.* **2020**, *49*, 7968–7976.

[53] A. Bhanja, R. Herchel, Z. Travnícek, D. Ray, *Inorg. Chem.* **2019**, *58*, 12184–12198.

[54] A. Chakraborty, N. Ahmed, J. Ali, S. Moorthy, J. Goura, S. K. Singh, G. Rogez, V. Chandrasekhar, *Dalton Trans.* **2022**, *51*, 14721–14733.

[55] T. D. Pasatoiu, J.-P. Sutter, A. M. Madalan, F. Z. C. Fellah, C. Duhayon, M. Andruh, *Inorg. Chem.* **2011**, *50*, 5890–5898.

[56] K. S. Cole, R. H. Cole, *J. Chem. Phys.* **1941**, *9*, 341–351.

[57] R. Orbach, *Proc. R. Soc. London Ser. A* **1961**, *264*, 458–484.

[58] R. Orbach, *Proc. Phys. Soc.* **1961**, *77*, 821–826.

[59] B. Dutta, T. Guizouarn, F. Pointillart, K. Kotrle, R. Herchel, D. Ray. *Dalton Trans.* **2023**, *52*, 10402.

[60] A. Døssing, *Coord. Chem. Rev.* **2014**, *280*, 38-53.

[61] L. Belkhiri, B. Le Guennic, A. Boucekkine, *Magnetochemistry* **2019**, *5*, 15.

[62] F. Neese, *Coord. Chem. Rev*. **2009**, 253, 526-563.

[63] R. D. Shannon, *Acta Cryst. A* **1976**, 32, 751-767.
[64] A. E. Reed, L. A. Curtiss, F. Weinhold, *Chem. Rev*. **1988**, *88*, 899-926.
[65] I. Mayer, *Chem. Phys. Lett*. **1983**, *97*, 270-274.
[66] R. F. Nalewajski, J. Mrozek, *Int. J. Quantum Chem*. **1994**, *51*, 187.
[67] R.F. Nalewajski, J. Mrozek, A. Michalak, *Int. J. Quantum Chem*. **1997**, *61*, 589.
[68] (a) E. Cremades, S. Gómez-Coca, D. Aravena, S. Alvarez, E. Ruiz, *J. Am. Chem. Soc*. **2012**, *134*, 10532-10542. (b) S. K. Singh, N. K. Tibrewal, G. Rajaraman, *Dalton Trans.* **2011**, *40*, 10897-10906. (c) G. Rajaraman, F. Totti, A. Bencini, A. Caneschi, R. Sessoli, D. Gatteschi, *Dalton Trans.* **2009**, *17*, 3153-3161. (d) J. Miralles, O. Castell, R. Caballol, J. P. Malrieu, *Chem. Phys.* **1993**, *172*, 33-43. (e) A. Dey, J. Acharya, V. Chandrasekhar, *Chem. Asian J.* **2019**, *14*, 4433-4453.
[69] J. H. Wang, P. F. Yan, G. M. Li, J. W. Zhang, P. Chen, M. Suda, Y. Einaga, *Inorg. Chim. Acta.* **2010**, *363*, 3706-3713.
[70] J.-P. Costes, F. Dahan, A. Dupuis, J.-P. Laurent *Inorg. Chem.* **1997**, *36*, 4284-4286.
[71] P. J. Hay, J. C. Thibeault, R. Hoffmann, *J. Am. Chem. Soc*. **1975**, *97*, 4884-4899.
[72] S. G. McAdams, A-M. Ariciu, A. K. Kostopoulos, J. P. S. Walsh, F. Tuna, *Coord. Chem. Rev.* **2017**, *346*, 216-239.
[73] J. Cirera, Y. Jiang, L. Qin, Y.-Z. Zheng, G. Li, G. Wu, E. Ruz, *Inorg. Chem. Front.* **2016**, *3*, 1272-1279.
[74] (a) M. Andruh, I. Ramade, E. Codjovi, O. Guillou, O. Kahn, J. C. Trombe, *J. Am. Chem. Soc.* **1993**, *115,* 1822-1829. (b) I. Ramade, O. Kahn, Y. Jeannin, F. Robert, *Inorg. Chem.* **1997**, *36*, 930-936.
[75] G. M. Sheldrick, *Acta Cryst. A* **2015**, *71*, 3-8.
[76] G. M. Sheldrick, *Acta Cryst. C* **2015**, *71*, 3-8.
[77] P. V. D. Sluis, A.L. Spek, *Acta Cryst*. *A* **1990**, *46*, 194-201.
[78] A. L. Spek, *J. Appl. Cryst.* **2003**, *36*, 7-13.
[79] M. Nardelli, *J. Appl. Cryst.* **1999**, *32*, 563-571.
[80] G. te Velde, F. M. Bickelhaupt, E. J. Baerends, C. Fonseca Guerra, S. J. A. van Gisbergen, , J. G. Snijder, T. Ziegler, *J. Comput. Chem.* **2001**, *22*, 931-967.
[81] R. Rüger, M. Franchini, T. Trnka, A. Yakovlev, E. van Lenthe, P. Philipsen, T. van Vuren, B. Klumpers, T. Soini. Amsterdam Modeling Suite (AMS version: 2021.107), Software for Chemistry & Materials SCM, Theoretical Chemistry, Vrije Universiteit, Amsterdam, The Netherlands, http://www.scm.com
[82] E. van Lenthe, E. J. Baerends, J. G. Snijders, *J. Chem. Phys*. **1993**, *99*, 4597-4610.
[83] E. van Lenthe, A. E. Ehlers, E. J. Baerends, *J. Chem. Phys*. **1999**, *110*, 8943-8953.
[84] L. Belkhiri, R. Maurice, B. Le Guennic, A. Boucekkine, M. Ephritikhine, *Eur. J. Inorg. Chem.* **2024**, 27, e202300788.
[85] S. Ouilia, C. Beghidja, A. Beghidja, L. Belkhiri, P. Rabu, *Inorg. Chim. Acta*. **2018**, 476, 54-59.
[86] A. D. Becke, *Phys. Rev. A* **1988**, *38*, 3098-3100.
[87] J. P. Perdew, *Phys. Rev. B* **1986**, *33*, 8822-8824.
[88] A. D. Becke, *Chem. Phys*. **1993**, 98, 5648-5652.
[89] C. Lee, W. Yang, R. G. Parr, *Phys. Rev. B* **1988**, *37*, 785-789.
[90] S. H. Vosko, L. Wilk, M. Nusair, *Can. J. Phys.* **1980**, 58, 1200-1211.
[91] P. J. Stephens, F. J. Devlin, C. F. Chabalowski, M. J. Frisch, *J. Phys. Chem.* **1994**, 98, 11623-11627.
[92] C. Adamo, V. Barone, *J. Chem. Phys*. **1999**, 110, 6158-6169.
[93] J. P. Perdew, M. Ernzerhof, K. Burke, *J. Chem. Phys.* **1996**, 105, 9982-9985.
[94] G. te Velde, F. M. Bickelhaupt, E. J. Baerends, C. Fonseca Guerra, S. J. A. van Gisbergen, , J. G. Snijder, T. Ziegler, *J. Comput. Chem.* **2001**, *22*, 931-967.
[95] L. J. Noodleman, E. R. Davidson, *J. Chem. Phys*. **1986**, *109*, 131–143.
[96] L. J. Noodleman, C. Y. Peng, D. A. Case, J. M. Mouesca, *Coord. Chem. Rev*. **1995**, *144*, 199-244.
[97] K. Yamaguchi, F. Jensen, A. Dorigo, K.N. Houk, *Chem. Phys. Lett*. **1988**, *149*, 537-542.
[98] T. Onishi, D. Yamaki, K. Yamaguchi, Y. Takano, *J. Chem. Phys*. **2003**, *118*, 9747−9761.
[99] M. Shoji, K. Koizumi, Y. Kitagawa, T. Kawakami, S. Yamanaka, Okumura, M. Yamaguchi, *Chem. Phys. Lett.* **2006**, *432*, 343−347.

.

## Entry for the Table of Contents

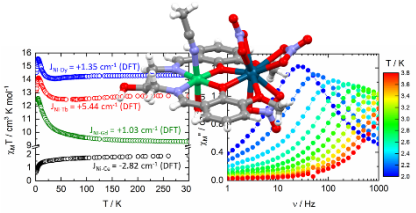


Four 3d4f heterobimetallic Schiff Base complexes were designed from the ditopic N, N'-bis(3-methoxysalicylaldiimine)-1,3-propylene-2-ol ligand. Experimental dc magnetic measurements and DFT computational investigations converged to antiferromagnetic exchange interaction between Ni(II) and Ce(III) ions while ferromagnetic interaction operated for Ln(III) = Gd, Tb and Dy. The latter displayed Single-Molecule Magnet behaviour.